JACS
JOURNAL OF THE AMERICAN CHEMICAL SOCIETY
Article
pubs.acs.org/JACS

Rapid Hydrogen and Oxygen Atom Transfer by a High-Valent Nickel–Oxygen Species

Teresa Corona,[†] Apparao Draksharapu,[‡] Sandeep K. Padamati,[‡] Ilaria Gamba,[†] Vlad Martin-Diaconescu,[†] Ferran Acuña-Parés,[†] Wesley R. Browne,[‡] and Anna Company*[,†]

[†]Grup de Química Bioinspirada, Supramolecular i Catàlisi (QBIS-CAT), Institut de Química Computacional i Catàlisi (IQCC), Departament de Química, Facultat de Ciències, Universitat de Girona, C/ Maria Aurèlia Capmany 69, E17003 Girona, Catalonia, Spain

[‡]Molecular Inorganic Chemistry, Stratingh Institute for Chemistry, Faculty of Mathematics and Natural Sciences, University of Groningen, Nijenborgh 4, 9747 AG Groningen, The Netherlands

Supporting Information

ABSTRACT: Terminal high-valent metal–oxygen species are key reaction intermediates in the catalytic cycle of both enzymes (e.g., oxygenases) and synthetic oxidation catalysts. While tremendous efforts have been directed toward the characterization of the biologically relevant terminal manganese–oxygen and iron–oxygen species, the corresponding analogues based on late-transition metals such as cobalt, nickel or copper are relatively scarce. This scarcity is in part related to the "Oxo Wall" concept, which predicts that late transition metals cannot support a terminal oxido ligand in a tetragonal environment. Here, the nickel(II) complex (**1**) of the tetradentate macrocyclic ligand bearing a 2,6-pyridinedicarboxamidate unit is shown to be an effective catalyst in the chlorination and oxidation of C–H bonds with sodium hypochlorite as terminal oxidant in the presence of acetic acid (AcOH). Insight into the active species responsible for the observed reactivity was gained through the study of the reaction of **1** with ClO^- at low temperature by UV–vis absorption, resonance Raman, EPR, ESI-MS, and XAS analyses. DFT calculations aided the assignment of the trapped chromophoric species (**3**) as a nickel-hypochlorite species. Despite the fact that the formal oxidation state of the nickel in **3** is +4, experimental and computational analysis indicate that **3** is best formulated as a Ni^{III} complex with one unpaired electron delocalized in the ligands surrounding the metal center. Most remarkably, **3** reacts rapidly with a range of substrates including those with strong aliphatic C–H bonds, indicating the direct involvement of **3** in the oxidation/chlorination reactions observed in the **1**/ClO^-/AcOH catalytic system.

INTRODUCTION

Terminal high-valent metal–oxygen species are key reaction intermediates in the catalytic cycles of both enzymes (e.g., oxygenases) and synthetic oxidation catalysts.[1−5] Many examples of natural and synthetic terminal high-valent Fe-oxygen, and Mn-oxygen species have been reported in the past decade.[6,7] In sharp contrast, and despite some efforts, detection of terminal high-valent metal–oxygen species involved in the mode of action of highly efficient oxidation catalysts based on late-transition metals such as cobalt, nickel or copper are scarce. This is in part related to the "Oxo Wall" concept, which predicts that late transition elements cannot support a terminal oxido ligand in a tetragonal environment.[8,9] Elucidating the mechanisms by which reactions catalyzed by late transition metal complexes proceed is essential for the rational development of selective catalytic reagents based on these metals, and requires a comprehensive understanding of the structure and properties of the key reactive species. It is only in recent years that the structural, spectroscopic and reactivity of well-defined oxido-cobalt(IV),[10,11] hydroxido-cobalt(III),[12] hydroxido-copper(III),[13] oxido/hydroxido-nickel(III)[14] and bicarbonate-nickel(III)[15] have been reported. Indeed, we reported earlier the formation of a metastable oxyl-nickel(III) species.[16] In all of these examples, highly basic ligand structures are necessary to stabilize the uncommonly high oxidation states of the metal center: either neutral guanidine-based ligands or the inclusion of a 2,6-pyridinedicarboxamidate unit in the ligand architecture were necessary. In particular, carboxamidate groups have proven to be a highly successful structural motif to support well-defined high-valent metal species including metal–oxygen compounds.[17−21]

Selected nickel complexes have been proven to be efficient catalysts in the challenging oxidation of alkanes and alkenes. For example, $[Ni^{II}(OAc)(tpa)(H_2O)]^+$ (tpa = tris(pyridylmethyl)amine) and related systems[22−24] catalyze the oxidation of alkanes with *m*CPBA or H_2O_2 as oxidant, while Ni-salen complexes[25,26] and Ni^{II} salts[27] have been successfully applied as catalysts in alkene epoxidation in combination with NaOCl. For hypochlorite-based nickel-mediated oxidations,

Received: July 21, 2016
Published: September 6, 2016

DOI: 10.1021/jacs.6b07544
J. Am. Chem. Soc. 2016, 138, 12987−12996

relatively little insight into the nature of the active species involved is available. Only recently, the complex $[Ni^{II}(CF_3SO_3)_2(Pytacn)]$ (Pytacn = 1-(2-pyridylmethyl)-4,7-dimethyl-1,4,7-triazacyclononane) was reported to catalyze alkane chlorination with NaOCl. Although several higher valent Ni^{III} species were observed, the role of the catalyst was concluded to be primarily to accelerate the formation of chlorine radicals through O−Cl bond cleavage via a spectroscopically characterized Ni^{II}−OCl species.[28]

Recently, we reported the formation of a metastable oxylnickel(III) species, $[Ni^{III}(O\bullet)(L)]$, by reaction of a nickel(II) precursor (**1**) with peracids at low temperature,[16] in which a macrocyclic tetradentate ligand (L) based on a 2,6-pyridinedicarboxamidate unit supported the metal center (Scheme 1). The $[Ni^{III}(O\bullet)(L)]$ was only sufficiently stable

Scheme 1. Previously Reported Reaction of 1 with *m*CPBA to Form $[Ni^{III}(O\bullet)(L)]$[16] along with the Reaction Studied in This Work

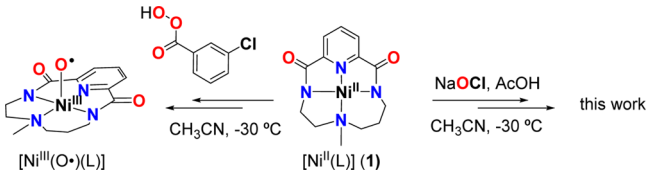

to be observed at subambient temperatures (<250 K) and reacted readily with organic substrates (C−H bonds, C−C double bonds and sulfides). Here, we show that reaction of **1** with NaOCl affords a new high valent Ni-OCl intermediate, which is characterized spectroscopically and by theoretical methods. The kinetic competence of this species in hydrogen-atom abstraction and oxygen-atom transfer reactions is demonstrated by unprecedentedly high reaction rates with a range of substrates.

RESULTS AND DISCUSSION

Catalytic Oxidation/Chlorination of Alkanes by 1 and NaOCl. Compound **1** was found to be a particularly efficient catalyst in the oxidation/chlorination of alkanes bearing strong C−H bonds (Table 1). Thus, addition of 100 equiv NaOCl into an MeCN solution containing 1 equiv **1** (1 mol % with respect to the oxidant), 100 equiv of AcOH and excess cyclohexane (300 equiv) afforded after stirring for 2 h under N_2 34 ± 4 TON (turnover number) of chlorocyclohexane and 7 ± 1 TON of cyclohexanone (entry 1). Interestingly, the yield significantly increased when the temperature was lowered down to −30 °C affording 44 ± 3 TON chlorocyclohexane and 9 ± 2 TON cyclohexanone, indicating that unproductive reaction pathways were occurring at higher temperatures (entry 3). Importantly, experiments in the absence of compound **1** or acetic acid afforded significantly lower yields (entries 4−6), indicating that all the reagents were necessary to efficiently catalyze this transformation. In order to evaluate the synthetic usefulness of this protocol, we carried out an experiment in which full conversion of the substrate could be achieved. The use of stoichiometric amounts of oxidant and cyclohexane caused a decrease in turnover numbers to 17 and 83% of substrate was not converted into products. Finally, *n*-hexane was also used as a substrate and 2-chlorohexane and 3-chlorohexane were obtained as the main products in a roughly 1:1 ratio. Remarkably, turnover numbers obtained for the present system are higher than those previously reported for alkane chlorination/oxidation reactions catalyzed by $[Ni^{II}(Pytacn)(CF_3SO_3)_2]$ or Mn(porphyrin) systems using NaOCl.[28,29] Insight into the nature of the active species involved in the oxidation/chlorination was gained through monitoring the reaction of **1** with NaOCl and AcOH in MeCN by UV−vis absorption spectroscopy at −30 °C, which unraveled the formation of two transient species, namely **2** and **3** (see below).

UV−vis Spectroscopic Detection of 2 and 3. Addition of 5 equiv AcOH to a solution of **1** (0.2 mM) did not alter its UV−vis absorption spectrum. Subsequent addition of 3 equiv ClO^- (either NaOCl or $Ca(OCl)_2$) induced an immediate decay of the absorption bands associated with **1** and the formation of a new species (**2**) with weak absorption bands at 550 and 650 nm ($\varepsilon \sim 500\ M^{-1}\ cm^{-1}$). Further addition of ClO^- up to 5 equiv. led to the appearance of an intensely colored species (**3**) with λ_{max} at 475 nm ($\varepsilon = 8000\ M^{-1}\ cm^{-1}$) and a decay half-life ($t_{1/2}$) of 4.2 h. Five equivalents of ClO^- and AcOH were found to be the optimal amounts to achieve maximum formation of **3** (Figure 1). In the absence of either ClO^- or AcOH species **2** and **3** were not formed, and, in

Table 1. Catalytic Chlorination and Oxidation of Cyclohexane and *n*-Hexane by 1 Using NaOCl/AcOH in MeCN[a]

entry	catalyst **1** (equiv)	AcOH (equiv)	substrate/equiv	*T* (°C)	$TON_{chlorination}$[b]	$TON_{oxidation}$[c]	TON_{total}[d]
1	1	100	cyclohexane/300	+25	34 ± 4	7 ± 1	41
2	0	100	cyclohexane/300	+25	14 ± 1	0	14
3	1	100	cyclohexane/300	−30	44 ± 3	9 ± 2	53
4	0	100	cyclohexane/300	−30	12 ± 2	0	12
5[e]	1	0	cyclohexane/300	−30	11 ± 2	6 ± 1	17
6[e]	0	0	cyclohexane/300	−30	4 ± 1	0	4
7	1	100	cyclohexane/100	−30	15 ± 2	2 ± 1	17
8	0	100	cyclohexane/100	−30	7 ± 2	0	7
9	1	100	*n*-hexane/300	−30	21 ± 3	8 ± 2	29
10	0	100	*n*-hexane/300	−30	4 ± 2	4 ± 2	8

[a]Reaction conditions: in typical reaction, 0.1 mL of a 0.5 M solution of AcOH (50 μmol) in MeCN and 32 μL of commercially available NaOCl 10 wt % (50 μmol) were added to a vigorously stirred MeCN solution (2.5 mL) containing compound **1** (0.5 μmol) and the substrate (50 or 150 μmol) under N_2. The mixture was stirred for 2 h. All reactions were run in duplicate. For more details, see the Experimental Section. [b]$TON_{chlorination}$ = turnover number of chlorinated products. Chlorocyclohexane for the oxidation of cyclohexane and a 1:1 mixture of 2-chlorohexane and 3-chlorohexane for *n*-hexane. [c]$TON_{oxidation}$ = turnover number of ketone products. Cyclohexanone for the oxidation of cyclohexane and a 1:1 mixture of 2-hexanone and 3-hexanone for *n*-hexane. [d]$TON_{total} = TON_{chlorination} + TON_{oxidation}$. [e]No acetic acid used.

DOI: 10.1021/jacs.6b07544
J. Am. Chem. Soc. 2016, 138, 12987−12996

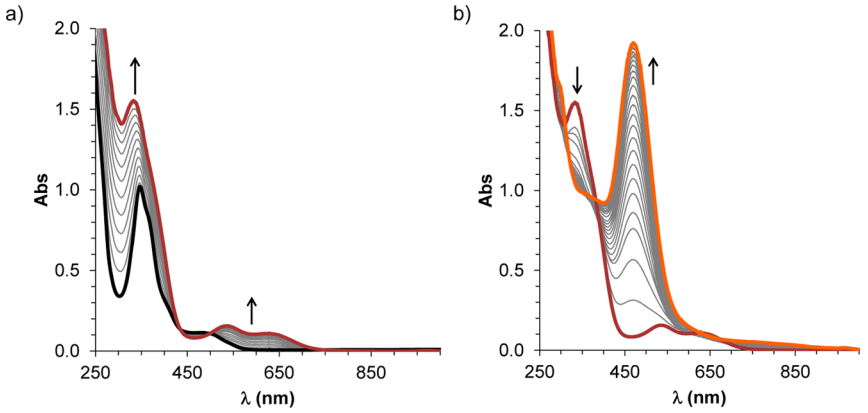

Figure 1. UV−vis absorption spectrum of **1** over time with a two-step addition of $Ca(OCl)_2$ at −30 °C in MeCN:H_2O 95:5 (v:v). (a) Step 1: 3 equiv ClO^- added to **1** (0.2 mM, black line) in MeCN in the presence of 5 equiv AcOH resulted in the formation of species **2** (red line). (b) Step 2: addition of a further 2 equiv ClO^- to **2** (red line) resulted in the formation of **3** (orange line). Equivalent results were obtained with the use of NaOCl.

addition, it was noted that with excess of AcOH the rate of formation of **3** was increased significantly.

The involvement of **2** and **3** in oxidation/chlorination of organic substrates was explored. Addition of organic substrates to a solution containing **2** had no effect on its UV−vis absorption spectrum; its characteristic absorption bands were not changed. In contrast, compound **3** reacted rapidly with alkanes, alkenes and sulfides. The spectroscopic characterization of these two species as well as the reactivity of **3** toward organic substrates will be discussed in the following sections.

Spectroscopic Characterization of 2. UV−vis absorption spectroelectrochemistry was used to gain information about the possible formulation of compound **2**. Thus, the spectroelectrochemical oxidation of **1** confirmed that the quasi-reversible redox wave ($I_{pa}/I_{pc} \sim 1$, $\Delta E \sim 70$ mV at a scan rate of 100 mV·s^{-1}) at $E_{1/2}$ 0.90 V vs Ag/AgCl (Figure S1), assigned to the Ni^{III}/Ni^{II} redox couple, was also fully reversible chemically. Electrochemical oxidation of **1** at 0.96 V in MeCN resulted in a change in its UV−vis absorption spectrum (λ_{max} 343 nm, ε = 4000 M^{-1} cm^{-1}) to that of a new species with an absorption band at λ_{max} 850 nm corresponding to $[Ni^{III}(L)]^+$ (**1**$^+$). The original absorption spectrum was fully recovered by subsequent reduction at 0.85 V (Figure S2). A similar result was obtained when water (50 equiv) and acetic acid (5 equiv) were present in the reaction medium. Remarkably, when the same experiment was performed in the presence of not only water and acetic acid but also NaCl (5 equiv), the resulting UV−vis spectrum matched well the UV−vis absorption features measured for **2** with weak absorption bands at λ_{max} ~550 and ~650 nm (Figure S3). This process could be reversed and the spectrochemical reduction of the formed species led to the recovery of the UV−vis spectrum of **1**. These data strongly support the assignment of **2** as $[Ni^{III}(L)(Cl)]$.

EPR analysis further supported this assignment. Thus, the EPR spectrum obtained from a flash frozen (77 K) solution, obtained by mixing **1** with 5 equiv AcOH and 3 equiv NaOCl in MeCN:H_2O 95:5 at −30 °C to form **2**, exhibited a signal characteristic of an axial $S = 1/2$ Ni^{III} species with $g_\perp = 2.23$ and $g_\parallel = 2.01$ which accounted for 65% of the nickel content (Figure S4).[30,31] The formulation of **2** as $[Ni^{III}(L)(Cl)]$ also fully agreed with the results obtained by cryospray ionization mass spectrometry (CSI-MS) at −30 °C. MS analysis of **2** revealed a simple spectrum with a major signal at m/z 318.0588, with a m/z value and isotopic pattern fully consistent with $[Ni^{III}(L)]^+$ in agreement with the +3 oxidation state of the nickel center determined by EPR spectroscopy (Figure S5). Finally, XAS analysis of **2** further supported the presence of a mononuclear nickel center coordinated to an apical chloride ligand (see XAS analyis below).

Kinetic Analysis of the Reaction of 3 with Organic Substrates. In contrast to species **2**, compound **3** reacted rapidly with different substrate types including alkanes, alkenes and sulfides. Under conditions of excess substrate, the decay of the absorption band of **3** (λ_{max} = 475 nm) was pseudo-first-order and fitted a monoexponential function from which observed rate constants (k_{obs}) were extracted (Figure S6, S8). Reaction rates were found to be the same within error under N_2 or air. The linear variation of k_{obs} with substrate concentration enabled calculation of second-order rate constants (k, Figure S7, S9, S10, and Table S1). Interestingly, **3** was kinetically competent in the reactions with alkanes bearing C−H bonds as strong as those of cyclohexane (bond dissociation energy, BDE, of 99.3 kcal·mol^{-1}), and a k = 0.0011 M^{-1} s^{-1} was determined for this substrate. Second order rate constants corrected by the number of C−H bonds in the substrate (k') for the reaction of **3** with various alkanes bearing C−H bonds with BDEs ranging from 75.5 to 99 kcal·mol^{-1} were determined. Log(k') values correlated linearly with the BDE values of the substrates, giving a slope of approximately −0.3 (Figure 2a). This correlation together with a KIE of 1.5 determined for the oxidation of 9,10-dihydroanthracne (Figure S11) indicates that **3** reacts with

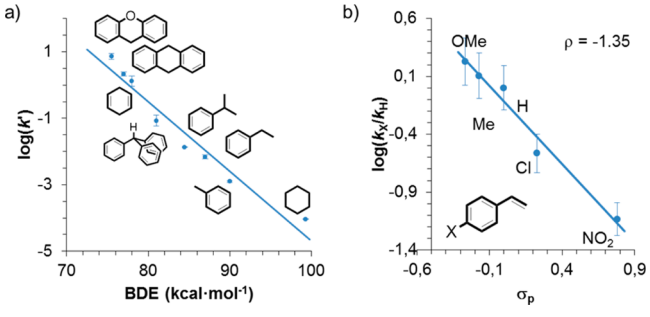

Figure 2. (a) Plot of log(k') against the C−H BDE for the reaction of **3** toward several alkanes in MeCN:H_2O 95:5 (v:v) at −30 °C. (b) Hammett plot for the reaction of **3** against *para*-substituted styrenes in MeCN:H_2O 95:5 (v:v) at −30 °C.

DOI: 10.1021/jacs.6b07544
J. Am. Chem. Soc. 2016, 138, 12987−12996

alkanes in a rate-determining hydrogen-atom abstraction step. Such behavior is consistent with that observed for the $[Ni^{III}(O•)(L)]$ species previously reported by us,[16] albeit the reactivity of **3** is substantially greater (Table 2). Analysis of the

Table 2. Second-Order Rate Constants (k) for the Oxidation of Alkanes, Alkenes and Thioethers by 3 or $[Ni^{III}(O•)(L)]$ in MeCN:H_2O 95:5 (v:v) at −30 °C

	k, M^{-1} s^{-1}	
	3	$[Ni^{III}(O•)(L)]$[16]
xanthene	14	2.93
9,10-dihydroantrhacene	8.5	2.62
1,4-cyclohexadiene	5.5	1.69
fluorene	–	0.28
styrene	4.1	0.45
cyclooctene	73	0.18
thioanisole	>100	0.56
1-octene	0.45	0.044

final oxidation products for the reaction of **3** with triphenylmethane indicated the formation of 1.4 TON of products consisting mainly of triphenylchloromethane together with small amounts of triphenylmethanol. Most of these products originated from a nickel-mediated process as ascertained by a blank experiment in the absence of nickel, which exclusively afforded 0.5 TON of chlorinated product (Table S2).

Compound **3** could also engage in oxygen-atom transfer (OAT) reactions. The rate of the reaction of **3** with 1-octene was 0.45 M^{-1} s^{-1}, which is an order of magnitude greater than that determined at the same temperature for $[Ni^{III}(O•)(L)]$. Similarly, reaction of **3** with other olefins, such as styrene or cyclooctene, were between 100 and 500 times faster than for $[Ni^{III}(O•)(L)]$ (Table 2). The electrophilic character of **3** was evidenced by the dependence of the reaction rates on the nature of the *para*-substitutent in a series of styrenes. A Hammett analysis of these reactions rates afforded a negative reaction constant (ρ) of −1.35 (Figure 2b), which indicates the electrophilic character of **3** in OAT reactions.[32] Remarkably, the reaction of **3** with thioanisole was too rapid to extract accurate kinetic data at −30 °C using our conventional UV−vis absorption spectrophotometer. Overall, the data indicate that **3** is a highly active oxidizing species with much greater reactivity than previously reported nickel systems[14,15,33] including the $[Ni^{III}(O•)(L)]$ species that bears the same ligand as **3**.[16] Similarly to the reaction with alkanes, analysis of the oxidized products after reaction of **3** with alkenes and sulfides proved that, indeed, this species mediated an oxygen-atom transfer reaction (Table S2). Thus, 1,2-epoxyoctane was formed in the reaction of 1-octene with **3** in 20% yield (with respect to nickel), while no epoxide product was detected in a blank experiment in the absence of nickel. In the case of thioanisole, the exclusive formation of 1.3 TON sulfoxide product was determined in the reaction with **3**, but only 0.3 TON were obtained in the corresponding blank experiment.

Spectroscopic Characterization of 3. Spectroscopic analysis provided insight into the chemical nature of **3**. Analysis of frozen solutions of **3** in MeCN (77 K) by Raman spectroscopy at 473 nm showed resonance enhancement of two bands, which tracked the appearance and disappearance of the visible absorption of **3** (λ_{max} 475 nm), at 703 and 443 cm^{-1} (Figure 3 and S12). ^{18}O-labeling using $Na^{18}OCl$ resulted in a downshift to 679 and 435 cm^{-1}. By comparison to previously

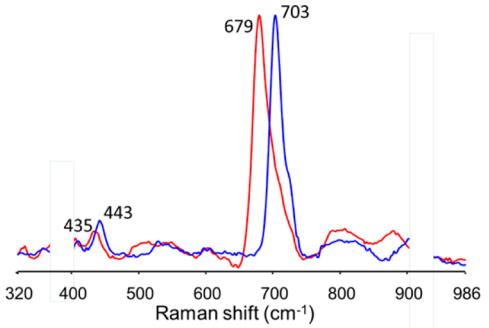

Figure 3. Resonance Raman spectra (λ_{exc} 473 nm) in frozen MeCN:H_2O 95:5 (v:v) (77 K) of **3** formed after reaction of **1** (0.48 mM) in MeCN:H_2O 95:5 (v:v) at −30 °C with 5 equiv AcOH and 5 equiv NaOCl (blue line) or 5 equiv $Na^{18}OCl$ (red line). Artifacts due to imperfect solvent subtraction were masked with white boxes.

reported Fe-OCl systems[34] these bands are assigned tentatively to O−Cl and Ni−O stretching modes, respectively. The observed shift of 24 cm^{-1} for the 703 cm^{-1} band is in good agreement with the calculated shift ($\Delta[^{18}O] = -29$ cm^{-1}) using the two-atom approximation for an O−Cl stretching mode, while the shift of 8 cm^{-1} for the 443 cm^{-1} indicates that this vibration is associated not only to the oxygen atom but also to ligand modes (expected shift for a Ni−O bond is $\Delta[^{18}O] = -20$ cm^{-1}). Importantly, both the resonantly enhanced bands at 703 and 443 cm^{-1} and the absorption band at 475 nm disappeared upon addition of 50 equiv 1-octene (Figure S13).

EPR analysis of a solution of **3** showed an EPR signal with g values $g_\perp$ = 2.23 and $g_\parallel$ = 2.01 assigned to compound **2**. However, this signal accounted for less than 30% of the overall nickel content, which indicated that compound **3** is EPR silent. CSI-MS analysis of **3** at −30 °C revealed a clean spectrum dominated by a peak at m/z 334.0585, which corresponds to $[Ni(O)(L)]^+$ (Figure 4). When compound **3** was generated using $Na^{18}OCl$, a shift of two mass units of the latter signal to m/z 336.0592 was observed (Figure 4 and S14). Collision induced dissociation (CID) experiments conducted over these signals at a collision energy of 20−25 eV afforded in both cases a new signal at m/z 317.05 indicative of the loss of an OH/^{18}OH radical (Figure S14 and S16). The fact that the signal at m/z 334.06 disappeared upon addition of substrate (1-octene) and that the oxygen atom is lost in CID experiments suggests that it does not originate from incorporation of oxygen into the ligand architecture, e.g., hydroxylation of methylenic C−H bonds in ligand L.

X-ray absorption spectroscopy (XAS) at the metal K-edge was applied to probe the electronic and geometric structure of the nickel center in **3**.[35−40] For comparison purposes, XAS on compound **2**, assigned as $[Ni^{III}(L)(Cl)]$ (see above), was also performed. Figure 5 (left) shows an overlay of the XANES region of compounds **2** and **3** and the previously reported oxyl-Ni^{III} radical analog $[Ni^{III}(O•)(L)]$.[16]

The spectra of compounds **2** and **3** have similar rising edge profiles when compared to that of $[Ni^{III}(O•)(L)]$, indicating a similar square bipyramidal coordination geometry at the metal center.[39,40] However, for **2** the rising edge is 0.4 eV lower in energy than $[Ni^{III}(O•)(L)]$, with a half-height edge energy of 8343.0 eV, indicating a more electron rich metal center with a lower effective charge. On the other hand a shift to higher energy is observed for compound **3** with a rising edge at ∼8344.0 eV (Figure S17). A similar trend is also observed in

DOI: 10.1021/jacs.6b07544
J. Am. Chem. Soc. 2016, 138, 12987−12996

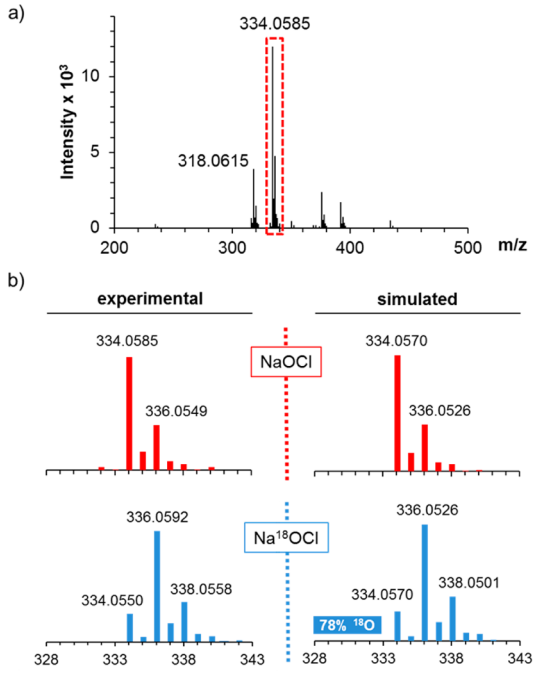

Figure 4. (a) CSI-MS of **3** at −30 °C formed by reaction of **1** with 5 equiv NaOCl in the presence of 5 equiv AcOH in MeCN:H_2O 95:5 (v/v) at −30 °C (equivalent spectra were obtained using 30 equiv NaOCl and 20 equiv AcOH). The spectrum shows major peaks at m/z 318.0615 and m/z 334.0585 corresponding to $[Ni(L)]^+$ and $[Ni(O)(L)]^+$, respectively. (b) Experimental and simulated pattern for the peak at m/z 334.06 formed with NaOCl (top) or partially ^{18}O-labeled NaOCl (bottom).

the pre-edges of **2** and **3**, associated with 1s → 3d transitions, where the pre-edge of **2** at 8333.15 eV indicates a more "effectively" reduced metal center and a weaker ligand field than in **3**, which has a pre-edge at 8333.54 similar in energy to that reported for $[Ni^{III}(O\bullet)(L)]$ at 8333.65 eV. The energies derived from the pre-edge analysis for the series are consistent with the presence of Ni^{III} centers, having pre-edges ∼1 eV higher in energy than those reported for Ni^{II}.[16,39,41] Additionally, a lower rising edge for **2** is consistent with the presence of the more electron donating Cl^- ligand in the coordination sphere of **2** versus oxygen-derived ligands in **3** and $[Ni^{III}(O\bullet)(L)]$. This is supported by EXAFS analysis of **2**, which confirms the presence of chloride in the coordination sphere of the Ni center (Figure 5 center, Table 3 and Table S3). In addition to the chloride, 4 N/O ligands are present as well as single and

Table 3. Comparison of EXAFS Determined and Density Functional Theory Derived Bond Metrics for Compounds 2 and 3[a]

	EXAFS					DFT
model	path[b]	r (Å)	σ^2 (×10³ Å²)	%R	χ^2_v	r (Å)
compound **2**	3 N/O	1.86(1)	2(1)	6.3	9.4	1.86
	1 N/O	2.07(3)	2(1)			1.93
	1 Cl	2.50(4)	7(5)			2.40
	8 C	2.72(1)	8(4)			2.76
compound **3**	5 N/O	1.89(1)	3(1)	7.5	3.9	1.93
	8 C	2.76(2)	5(2)			2.77

[a]Full scattering paths outlined in Tables S3–S4. [b]Chemical intuition was used to differentiate between N/C/O paths.

multiple scattering paths consistent with the presence of the macrocyclic ligand. Compound **3** was also characterized structurally using EXAFS analysis and shows a Ni center surrounded by a first coordination shell of 5 N/O ligands at 1.89 Å, accompanied by single and multiple scattering C/N paths at 2.77 and 2.96 Å (Figure 5 right, Table 3 and Table S4). This is consistent with a metal center surrounded by the macrocyclic ring of the ligand and coordinated by the 4 nitrogen atoms of the macrocycle in the equatorial plane with an additional axial N/O ligand. The EXAFS determined structures and bond distances for **2** and **3** are in agreement with the computational models proposed below (Table 3).

The possibility of dimerization to form Ni−X−Ni complexes was also explored using existing procedures including phase comparison and curve fitting.[37,42] Phase comparison revealed that the region of 3.4 to 3.8 Å in r-space, where Ni−Ni scattering paths should occur, is similar for all three complexes, while curve fitting of both **2** and **3** shows that inclusion of a Ni−Ni scattering path does not significantly improve the goodness of the fit, contributes to "overfitting" based on the χ^2_v parameter and results in unreasonable values for the disorder parameters (Figure S18). Therefore, EXAFS analysis does not support formation of Ni−X−Ni dimers. Lastly, previous reports have shown that in a series of Ni complexes with similar coordination environments a change of 0.7 eV in the rising edge is consistent with a +1 change in formal oxidation state.[39,43] Therefore, a change of ∼0.5 eV in the rising edge of **3** versus $[Ni^{III}(O\bullet)(L)]$ might indicate partial oxidation of the metal center and/or participation of the ligand sphere in the redox process.[44]

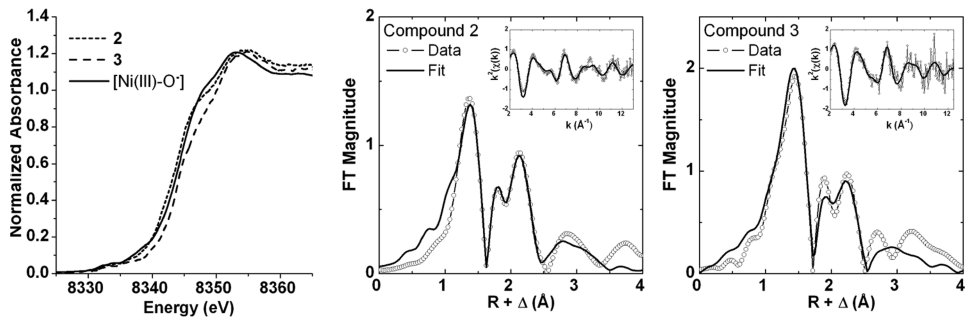

Figure 5. (Left) Comparison of the Ni K-edge XANES region for compounds **2**, **3** and $[Ni^{III}(O\bullet)(L)]$; (center) Fourier-transformed EXAFS spectra of **2** (no phase correction, FT, window = 2−13 $Å^{-1}$); (right) Fourier-transformed EXAFS spectra of **3** (no phase correction, FT, window = 2−12.5 $Å^{-1}$); Insets: k^2-weighted unfiltered EXAFS spectra.

DOI: 10.1021/jacs.6b07544
J. Am. Chem. Soc. 2016, 138, 12987−12996

Theoretical Models for Compound 3 and Correlation with Experiments. The nature of compound **3** was also explored by theoretical models and correlations were made to experimental data. The following evidences were taken into account: (i) resonance Raman indicates the presence of a Ni-OCl species in solution; (ii) CSI-MS experiments confirm the presence of a $[Ni(O)L]^+$ core; (iii) EPR spectroscopic data indicate that a $S = 1/2$ Ni^{III} species (**2**) is converted to compound **3**; (iv) XAS analysis is consistent with a monomeric high-valent Ni center surrounded by 5 N/O ligands in what is best described as a square pyramidal environment; (v) XANES analysis of the rising edge indicates a more oxidized metal center in **3** than in previously reported $[Ni^{III}(O\bullet)(L)]$,[16] albeit by only ~0.5 eV rather than 0.7 eV which would be expected for a formal +1 change in oxidation.

With all this information in hand, geometry optimizations of the nickel-OCl compound $[Ni(OCl)(L)]^+$ (**A**) in several possible spin states (S = 0, 1 or 2) were performed. The triplet multiplicity (^{3}**A**) was found to be the ground spin state, being 7 kcal·mol^{-1} more stable than the singlet (^{0}**A**). The model consists of a nickel center in a distorted square pyramidal geometry with the OCl ligand bound at the apical

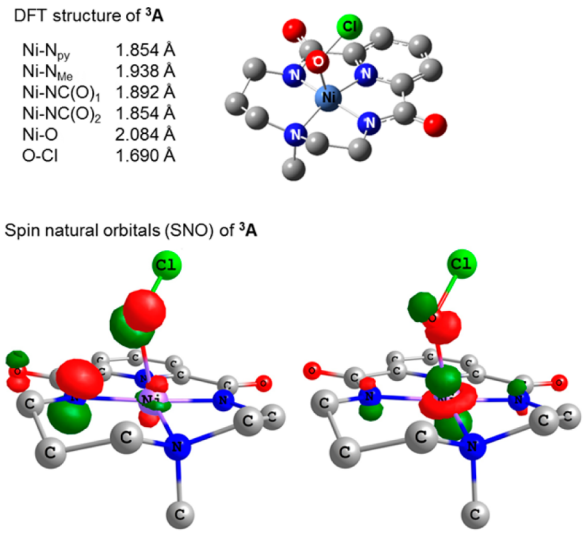

Figure 6. Top: DFT computed structure of ^{3}**A**. Bottom: Spin-natural orbitals (SNO) of ^{3}**A** (isovalue = 0.144).

position (Figure 6). Calculation of the free energy difference of ^{3}**A** relative to the starting reagents indicated that its formation is exergonic (ΔG = −12.8 kcal·mol^{-1}) (Figure 7).[45] We also considered the involvement of the corresponding 1e$^-$ reduced compound $[Ni(OCl)(L)]$ (**B**). However, formation of the most stable spin state of this species (^{2}**B**) from **1** was endergonic (ΔG = +5.3 kcal·mol^{-1}), and thus, the 1e$^-$ oxidized ^{3}**A** species is preferred on the basis of theoretical results (Figure 7, see Supporting Information for further details).

The free energy cost to cleave the O−Cl bond in ^{3}**A** was also determined. Heterolytic O−Cl cleavage to liberate Cl^- would lead to $[Ni(O)(L)]^{2+}$ in which the nickel center would be found in a formal +6 oxidation state, which is highly unlikely and thus, it was discarded. Instead, homolytic O−Cl cleavage would afford $[Ni(O)(L)]^+$ (**C**). However, the computed free energy for the conversion of ^{3}**A** to the most stable quadruplet **C** species (^{4}**C**) revealed a highly endergonic process (ΔG = +43.1

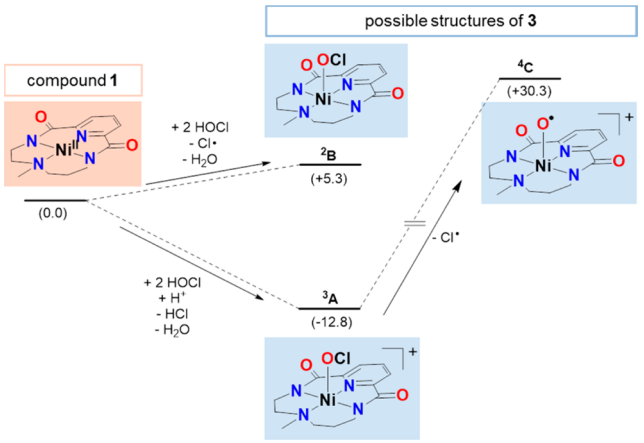

Figure 7. Possible formulations of compound **3** (**A**, **B** or **C**) derived from the reaction of **1** with NaOCl in the presence of AcOH. Free energies are given in parentheses in kcal·mol^{-1} at −30 °C in MeCN.

kcal·mol^{-1}) (Figure 7). Thus, O−Cl cleavage to form a nickel-oxido/oxyl species is disfavored on a thermodynamic basis, thus reinforcing the assignment of compound **3** as $[Ni(OCl)(L)]^+$ (^{3}**A**).

The proposed coordination geometry and bond distances of the ^{3}**A** theoretical model (Figure 6) are consistent with the experimentally derived geometry and bond metrics from XAS analysis (Table 3). Similarly, compound **2**, which is assigned as $[Ni^{III}(L)(Cl)]^+$ on the basis of several spectroscopic techniques (see above), was also modeled. A similar square pyramidal geometry to **3**, but having the ClO^- apical ligand replaced by Cl^-, and a $S = 1/2$ spin state was found to be the most stable configuration for **2** (Figure S21). This geometry was found to be almost isoenergetic with the starting complex **1**. Again, calculated bond distances for **2** agree, within error, with the experimentally derived bond distances (Table 3).

Additionally, TD-DFT calculated pre-edge XAS energies follow the observed experimental trends with **2** having the lowest energy calculated pre-edge, followed by **3** (~0.4 eV higher) and $[Ni^{III}(O\bullet)(L)]$ (~0.7 eV higher) (Figure S19a). The calculated pre-edge intensities are also consistent with experiment, with **2** and **3** having lower intensities than $[Ni^{III}(O\bullet)(L)]$ (Figure S19b). In all cases the pre-edges are predicted to have three metal based transitions (Figure S20). Difference density maps[46,47] of the pre-edge transitions highlight a core excitation to a singly occupied dz^2 orbital, which dominates the pre-edge intensities, followed by two transitions to the empty dx^2-y^2 orbital. The placement of the unpaired electron in the dz^2 orbital for **2** is also consistent with the EPR profile which suggests that the dz^2 orbital is the main contributor to the ground state.[15,48]

Furthermore, simulation of the Raman spectrum of ^{3}**A** (λ_{exc} at 473 cm^{-1}) predicts an intense O−Cl bond stretching at 701 cm^{-1} and a weaker Ni−O vibration at 406 cm^{-1} (Figure S22). This theoretically computed spectrum is in full agreement with the experimental data and the resonance enhanced bands at 703 and 443 cm^{-1}, for which ^{18}O-shifts to 679 and 435 cm^{-1} were observed. The small shift of the latter upon labeling ($\Delta[^{18}O]$ = −8 cm^{-1}) is due to the mixing of the Ni−O mode with ligand-based modes, as observed theoretically.

To better understand the effective oxidation state of the metal center and the electronic structure of ^{3}**A**, the spin populations around the metal center were investigated. Figure 6

DOI: 10.1021/jacs.6b07544
J. Am. Chem. Soc. 2016, 138, 12987−12996

shows the spin natural orbitals (SNO) for the two unpaired electrons in **3**. The figure illustrates a large extent of delocalization of spin between a proximal nitrogen (N_{ligand}), the Ni center and the OCl moiety. In fact the first SNO is composed primarily of N_{ligand} (~43%) and OCl π^* (~23%) character with only a minimal contribution from Ni (~8%) suggesting a ligand centered unpaired electron. The second SNO is composed mainly of Ni d_{z2} (62%) with 26% OCl π^* character. Mulliken spin population analysis further supports the location of the unpaired electrons (ρ(Ni) = 0.75, ρ(OCl) = 0.42 and $\rho(N_{ligand})$ = 0.55), which would suggest a Ni^{III} oxidation state at the metal center. This model is consistent with the XAS data, which shows a slightly more oxidized metal center in **3** than in the previously reported $[Ni^{III}(O\bullet)(L)]$ but not by a full formal oxidation unit. Moreover, the presence of an unpaired electron in an orbital with OCl π^* character might serve to activate the O−Cl bond and increase the reactivity of the complex. This would be consistent with the cleavage of the O−Cl bond in **3** under the MS conditions, which leads to the exclusive detection of $[Ni(O)(L)]^+$, in which the O−Cl bond of ^{3}**A** is homolytically broken, under the experimental conditions. Lastly, ligand radical character in the 2,6-pyridinedicarboxamidate ligand backbone (L) is not unexpected as pyridinecarboxamidate units may have noninnocent behavior in the presence of high valent metal centers.[49−51]

Overall, the computed structure for $[Ni(OCl)(L)]^+$ (^{3}**A**) is in agreement with the spectroscopic data obtained for **3** by EPR, rRaman, MS and XAS techniques. Despite the fact that the formal oxidation state of the nickel center in this compound is +4, our analyses indicate that its effective oxidation state is +3, with $1e^-$ oxidation distributed over the ligands.

■ CONCLUSIONS

In summary, the bis(amidate) macrocyclic ligand (L) acts as an excellent platform to support a high-valent nickel-hypochlorite species that has been trapped by reaction of the nickel(II) precursor with sodium (or calcium) hypochlorite in the presence of acetic acid at low temperatures. This compound has been characterized by UV−vis absorption and rRaman spectroscopy, XAS and cryospray mass analyses. DFT calculations indicate that this trapped species is best formulated as a formal nickel(IV) species with the formula $[Ni(OCl)(L)]^+$. Most interestingly, this species behaves as a strong oxidizing agent both toward alkanes and alkenes with reaction rates that surpass those previously reported for related nickel−oxygen species. Oxidation of C−H bonds as strong as those of cyclohexane has been achieved and the catalytic cyclohexane chlorination/oxidation has also been successfully performed. Overall, the involvement of high-valent nickel-OCl species in the catalytic cycle of nickel-catalyzed oxidation/chlorination reactions of alkanes and alkenes seems to be highly plausible. Current efforts in our group are devoted to study the influence of the electronic properties of the ligand on the high-valent nickel center and the use of ligand L in combination with other metals relevant to oxidation catalysis.

■ EXPERIMENTAL SECTION

Materials and Methods. Reagents and solvents used were commercially available and purchased from Panreac, Scharlau and Aldrich. Preparation and handling of air-sensitive materials were carried out in a N_2 drybox (MBraun ULK 1000) with O_2 and H_2O concentrations <1 ppm. $[Ni^{II}(L)]$ (**1**) was synthesized as previously reported.[16]

Mass spectra were performed by electrospray ionization in a high-resolution mass spectrometer Bruker micrOTOF QII (Q-TOF) with a quadrupole analyzer with positive and negative ionization modes. UV−vis absorption spectra were performed by a diode array spectrophotometer Agilent Cary 60 and low temperature control was maintained with a cryostat from Unisoku Scientific Instruments. GC analyses were carried out on an Agilent 7820A gas chromatograph (HP5 column, 30m) with a flame ionization detector. Raman spectra were recorded in 5 mm diameter NMR tubes at 77 K in a liquid nitrogen filled quartz Dewar. Spectra were collected in 180° backscattering mode with excitation at 473 nm (Cobolt Lasers, 50 mW) with a dichroic mirror (Semrock) at 45° to the optical collection axis and a 25 mm diameter (75 mm focal length) planoconvex lens to focus the excitation beam and collect and collimate Raman scattering, which was passed through the dichroic and a long pass cut off filter (Semrock) before being focused at the entrance slits of a Shamrock 303i spectrograph with a 1200 l/mm grating blazed at 500 nm and a iDUS-420-BUEX2-DD CCD detector (Andor Technology). Spectral calibration was carried out using a 1:1 v/v mixture of MeCN and toluene. Spectra were processed using Andor Solis and Spectrum 10 (PerkinElmer). EPR spectra were recorded with an EMX nano spectrometer (bruker instruments). Reactions were monitored by UV−vis spectroscopy and 300 μL aliquots were frozen at 77 K. All measurements were performed at 110 K. Spectra were recorded at 9.63 GHz, with a microwave power of 0.31 mW and power attenuation 25.00 dB or microwave power of 3.1 mW and power attenuation 15.00 dB. Modulation amplitude was 4.00 gauss and modulation frequency 100 kHz. Each spectrum was collected as an average of three scans. Sample tubes were filled higher than the cavity dimension to guarantee an equally filled cavity for all measured samples. Simulations of EPR spectra was carried out using EasySpin software.[52] Cyclic voltammetry was performed using a model CHI760C Electrochemical Workstation (CH Instruments) in MeCN (0.1 M $TBAPF_6$) with a 3 mm diameter Teflon-shrouded glassy carbon working electrode (CH Instruments), a Pt wire auxiliary electrode, and an Ag/AgCl reference electrode. Potentials are reported ±10 mV. Spectroelectrochemistry was performed using an OTTLE cell[53] (a liquid IR cell modified with Infrasil windows and a platinum mesh working and counter electrode and a Ag wire reference electrode) mounted in a Specord600 UV−vis absorption spectrometer. Bulk electrolysis was carried out in a divided cell (ceramic frit separation) with a 5 mM soluction of **1** in MeCN containing 500 mM water, 25 mM acetic acid and 25 mM NaCl, with a carbon mesh working electrode, platinum mesh counter electrode and Ag/AgCl working electrode. Electrolysis was carried out at 0.9 V and conversion to Ni^{III} monitored by ex situ UV−vis absorption and EPR spectroscopy.

A 1 mM sample of **3** (prepared by reaction of **1** with 5 equiv of AcOH and 5 equiv of NaOCl in CH_3CN at −30 °C) was loaded into a 1 mm holder with Kapton tape windows and stored at liquid nitrogen temperatures until run. Data collection was carried out in fluorescence mode at the ESRF synchrotron beamline Spline-BM25A equipped with a Si(111) double crystal monochromator, an Optistat CF cryostat from Oxford Instruments and a 13 channel element detector. Samples were run at 90 K under anaerobic conditions using a Z-1 filter to reduce backscattering. A 2 mM sample of **2** (prepared by reaction of **1** with 5 equiv of AcOH and 3 equiv of NaOCl in CH_3CN at −30 °C) was similarly loaded into a 1 mm holder with Kapton tape windows and stored at liquid nitrogen temperatures until run at the SAMBA beamline from SOLEIL equipped with a Si(220) double crystal monochromator, a liquid helium cryostat (25 K) and a 36 channel element detector. Energy calibration was performed using the first inflection point of the X-ray absorption near edge structure (XANES) spectrum of nickel foil (E_{cal} of 8331.6 eV). Data reduction and normalization was carried out with the Athena software package using the AUTOBK algorithm. A R_{bkg} of 1.1 Å and a spline between a k of 1 and 13.5 $Å^{-1}$ was used for EXAFS extraction. The follow up EXAFS analysis was carried out with the Artemis software program using the IFEFFIT engine and FEFF6 code.[54−56] The k^2-weighted data was fit in r-space between 1.0 and 4.0 Å without phase correction having a k-range of 2.0−12.5 $Å^{-1}$ for **3** and a k-range of 2.0−13 $Å^{-1}$ for **2**, as well

DOI: 10.1021/jacs.6b07544
J. Am. Chem. Soc. 2016, 138, 12987−12996

as using a Hanning window (dk 2). Scattering paths were fit in terms of Δr_{eff} and σ^2, having a global ΔE_0 and a S_0 value set to 0.9 for all paths. Coordination number was explored using single scattering shells with fixed degeneracies which were then varied in integral steps.[57−59] To assess the goodness of fit from different models both the R_{factor} (% R) and the reduced χ^2 (χ^2_v) were minimized. While the R_{factor} is generally expected to decrease with the number of adjustable parameters, χ^2_v may eventually increase, indicating the model is overfitting the data.[60] Lastly, in order to extract intensities and energy positions the XANES spectra was fit using pseudo-Voigt functions while the edge jump was modeled via a cumulative Gaussian−Lorentzian sum function.

*Catalytic Experiments at −30 °C Using **1** as Catalyst and AcOH/NaOCl as Oxidant.* In a typical reaction, 0.1 mL of a 0.5 M solution of AcOH (50 μmol) in MeCN and 32 μL of commercially available NaOCl 10% (50 μmol) were added at −30 °C to a vigorously stirred MeCN solution (2.5 mL) containing the nickel catalyst (0.5 μmol) and the substrate (50 or 150 μmol) for 2 h under N_2. The final concentrations of reagents were 0.2 mM nickel catalyst, 20 mM AcOH, 20 mM NaOCl, and 20 or 60 mM substrate. $Na_2S_2O_3$ (500 μmols) dissolved in MeCN:H_2O 1:1 was added at this point to destroy unreacted NaOCl and biphenyl was added as internal standard. Nickel complex and the small quantities of water were removed by passing the solution through a short path of silica and $MgSO_4$. The products were then eluted with ethyl acetate (2 mL) and the resulting mixture was analyzed by GC-FID. The organic products were identified by comparison with authentic compounds and quantified using a calibration curve.

*Generation of **2**.* In a typical experiment, 2.5 mL of a 0.2 mM solution of **1** in MeCN were placed in a 1 cm path-length cuvette (0.5 μmol of **1**). The quartz cell was placed in the Unisoku cryostat of the UV−vis absorption spectrophotometer and cooled down to −30 °C. After reaching thermal equilibrium an UV−vis absorption spectrum of the starting complex was recorded. Then, 25 μL of a 0.1 M solution of AcOH in MeCN were added (5 equiv) followed by 30 μL of a 0.05 M solution of NaOCl in MeCN:water (4:1) (3 equiv). The formation of two equally intense bands at λ_{max} = 550 and 650 nm ($\varepsilon \sim 500$ M^{-1} cm^{-1}) was observed. **2** reached its maximum within 200 s.

*Generation of **3**.* In a typical experiment, 2.5 mL of a 0.2 mM solution of **1** in MeCN were placed in a 1 cm path-length cuvette (0.5 μmol of **1**). The quartz cell was placed in the Unisoku cryostat of the UV−vis absorption spectrophotometer and cooled down to −30 °C. After reaching thermal equilibrium an UV−vis absorption spectrum of the starting complex was recorded. Then, 25 μL of a 0.1 M solution of AcOH in MeCN were added (5 equiv) followed by 50 μL of a 0.05 M solution of NaOCl in MeCN:water (4:1) (5 equiv). The formation of a band at λ_{max} = 475 nm (ε = 8000 M^{-1} cm^{-1}) was observed. The formation of **3** reached its maximum within 400 s.

*Kinetic Analyses of the Reaction of **3** with Organic Substrates.* Once **3** was fully formed (see above) the appropriate amount of substrate dissolved in 100 μL MeCN was directly injected into the UV−vis cuvette. Substrate concentration was always in pseudo-first order excess with respect to **3** and reaction kinetics were monitored by following the decay of its absorption band at 475 nm. In all cases, a satisfactory fit was obtained for the disappearance of **3** using a single exponential, from which observed rate constants (k_{obs}) were extracted. The linear variation of k_{obs} with substrate concentration enabled the calculation of the second-order rate constants (k). In the particular case of toluene and cyclohexane reactions were extremely slow and k values were determined from two replicates at a single substrate concentration (0.36 M). The kinetic isotope effect (KIE) was obtained by dividing the reaction rates obtained for the reaction of **3** with 9,10-dihydroantrhacene and 9,10-dihydroanthracene-d_4.

*Preparation of ^{18}O-Labeled **3**.* ^{18}O-labeled **3** was prepared following a similar procedure to that described above for **3** but using $Na^{18}OCl$ instead of $Na^{16}OCl$. In turn, $Na^{18}OCl$ was obtained by stirring 10 μL of NaOCl in 30 μL $H_2{}^{18}O$ for 2 h at room temperature, following a reported synthetic procedure.[28]

Product Analyses. Once the formation of **3** reached its maximum, 150 μL of a MeCN solution containing the required amount of the desired substrate were added in the UV−vis cuvette. The decay of the band at 475 nm was monitored. After complete disappearance of the chromophore, reactions were quenched by the addition of 10 equiv $Na_2S_2O_3$ dissolved in MeCN:H_2O 1:1 with respect to initial NaOCl and biphenyl was added as internal standard. Nickel complex and the small quantities of water were removed by passing the solution through a short path of silica and $MgSO_4$. The products were then eluted with ethyl acetate (2 mL) and the resulting mixture was analyzed by GC-FID. The organic products were identified by comparison with authentic compounds and quantified using a calibration curve.

Computational Details. Density functional theory (DFT) calculations were performed with the Gaussian09 program package.[61] X-ray diffraction structure of [Ni^{II}(L)] (**1**) has been chosen as starting point for geometry optimizations with the B3LYP exchange-correlation functional[62,63] and the TZVP basis set.[64] Nickel species were considered in all possible spin states without symmetry constraints. The MeCN solvation effects were included in geometry optimizations through the SMD polarizable continuum model.[65] Dispersion effects were included in geometry optimizations with the Grimme's D_3 correction with Becke-Johnson damping function.[66]

Analytical Hessian calculations were performed at the same level of theory to (i) evaluate enthalpy and entropy corrections at 243.15 K and (ii) establish the nature of stationary points in solvent-phase, where minima have no imaginary frequencies. Nonresonant Raman spectral intensities of intermediate **3** were simulated at 77 K and with a laser excitation of 473 nm employing the GaussSum 3.0.[67] The shift in the O−Cl bond stretching frequency upon ^{18}O-labeling was determined modeling the Raman spectrum with an ^{18}O−Cl bond.

Mulliken spin densities and spin natural orbitals (SNO) were computed to rationalize the electronic structure of all nickel based intermediates. The atomic orbital contribution to the SNOs was evaluated with the Multiwfn 3.3.6 software.[68]

Gibbs energies (G) were evaluated with the following equation:

$$G = E_{TZVP}(SMD + D_3) + G_{corr} \quad (1)$$

where $E_{TZVP}(SMD + D_3)$ is obtained through single point calculations with the TZVP basis set on equilibrium geometries, including the solvation and dispersion effects, and G_{corr} is the thermal correction obtained from a thermo-statistical analysis at the B3LYP/SMD level.

The dissociation free energy change ($\Delta G°$) between an acid (AH) and its conjugate base (A^-) in solvent phase was calculated using the following equations:

$$\Delta G = G(A_s^-) + G(H_s^+) - G(AH_s) + \Delta G^* \quad (2)$$

$$G(H_s^+) = G(H_{gas}^+) + \Delta G_{solv}^{H+} \quad (3)$$

where $G(AH_s)$ and $G(A_s^-)$ are the standard free energies of the acid and its conjugate base, respectively. In MeCN solution, the free energy of the proton $G(H_s^+)$ is obtained from the solvation free energy of a proton in MeCN (ΔG_{solv}^{H+} = −260.2 kcal·mol^{-1})[65] and its gas-phase free energy ($G(H_{gas}^+)$ = −6.3 kcal·mol^{-1}).[66] In the free energy balance the standard state thermodynamic correction associated with the conversion from a standard-state of 1 M in the solvent phase and 1 atm in gas phase to 1 M in both phases was considered. Its value is 1.54 kcal·mol^{-1} at 243.15 K.

The ORCA software package 3.0.1[69] was used to calculate XAS pre-edges using previously reported procedures.[46,70,71] Spin unrestricted, time-dependent calculations for XAS spectra were carried out using the Tamm−Dancoff[72,73] approximation and up to 13 nonrelativistic roots were calculated to ensure saturation of transitions spanning the pre-edge and near edge region of Ni XAS K-edge spectra. The B3LYP functional was employed along with a TZVP[74] basis set and a conductor like screening model (COSMO[75]) using acetonitrile as solvent.

DOI: 10.1021/jacs.6b07544
J. Am. Chem. Soc. 2016, 138, 12987−12996

■ ASSOCIATED CONTENT

Supporting Information

The Supporting Information is available free of charge on the ACS Publications website at DOI: 10.1021/jacs.6b07544.

Cyclic voltammetry and spectroelectrochemistry of **1**, EPR spectroscopy of **2**, CSI-MS analysis of **2** and **3**, resonance Raman, XAS analysis of **2** and **3**, kinetic analysis of the reaction of **3** with substrates, and DFT calculations including Raman simulations, thermodynamic data, spin density analysis and Cartesian coordinates of optimized geometries. (PDF)

■ AUTHOR INFORMATION

Corresponding Author

*anna.company@udg.edu

Notes

The authors declare no competing financial interest.

■ ACKNOWLEDGMENTS

Financial support for this work was provided by the European Commission (FP7-PEOPLE-2011-CIG-303522 to A.C.). The MINECO of Spain is acknowledged for a Ramón y Cajal contract to A.C. and for CTQ2013-43012-P to A.C. F. A.-P. thanks Universitat de Girona for a predoctoral grant. W.R.B. acknowledges the European Research Council (ERC-2011-StG-279549) and the Ministry of Education, Culture and Science (Gravity program 024.001.035). X-ray absorption data was collected on beamline BM25-Spline at the European Synchrotron Radiation Facility (ESRF), Grenoble, France. We are grateful to the Local Contact at ESRF, Dr. Eduardo Salas Colera, for providing assistance in using the beamline. XAS data was also collected at the SOLEIL French National Synchrotron Facility, Saint-Aubin, France, where we would like to thank Dr. Landrot Gautier for his assistance. This work was performed (partially) in the framework of COST action CM1305 "Explicit Control Over Spin-states in Technology and Biochemistry (ECOSTBio)" (STSM reference: ECOST-STSM-CM1305-32120). The authors thank Dr. Carole Duboc for fruitful discussions on analysis and interpretation of EPR data.

■ REFERENCES

(1) Costas, M.; Mehn, M. P.; Jensen, M. P.; Que, L. *Chem. Rev.* **2004**, *104*, 939−986.

(2) Denisov, I. G.; Makris, T. M.; Sligar, S. G.; Schlichting, I. *Chem. Rev.* **2005**, *105*, 2253−2278.

(3) Yano, J.; Yachandra, V. *Chem. Rev.* **2014**, *114*, 4175−4205.

(4) Bertini, I.; Gray, H. B.; Stiefel, E. I.; Valentine, J. S. *Biological Inorganic Chemistry. Structure & Reactivity*; University Science Books: Sausalito, CA, 2007.

(5) Oloo, W. N.; Que, L. *Acc. Chem. Res.* **2015**, *48*, 2612−2621.

(6) Kleespies, S. T.; Oloo, W. N.; Mukherjee, A.; Que, L. *Inorg. Chem.* **2015**, *54*, 5053−5064.

(7) Chen, Z.; Yin, G. *Chem. Soc. Rev.* **2015**, *44*, 1083−1100.

(8) Gray, H. B.; Hare, C. R. *Inorg. Chem.* **1962**, *1*, 363−368.

(9) O'Halloran, K. P.; Zhao, C.; Ando, N. S.; Schultz, A. J.; Koetzle, T. F.; Piccoli, P. M. B.; Hedman, B.; Hodgson, K. O.; Bobyr, E.; Kirk, M. L.; Knottenbelt, S.; Depperman, E. C.; Stein, B.; Anderson, T. M.; Cao, R.; Geletii, Y. V.; Hardcastle, K. I.; Musaev, D. G.; Neiwert, W. A.; Fang, X.; Morokuma, K.; Wu, S.; Kögerler, P.; Hill, C. L. *Inorg. Chem.* **2012**, *51*, 7025−7031.

(10) Hong, S.; Pfaff, F. F.; Kwon, E.; Wang, Y.; Seo, M.-S.; Bill, E.; Ray, K.; Nam, W. *Angew. Chem., Int. Ed.* **2014**, *53*, 10403−10407.

(11) Pfaff, F. F.; Kundu, S.; Risch, M.; Pandian, S.; Heims, F.; Pryjomska-Ray, I.; Haack, P.; Metzinger, R.; Bill, E.; Dau, H.; Comba, P.; Ray, K. *Angew. Chem., Int. Ed.* **2011**, *50*, 1711−1715.

(12) Lacy, D. C.; Park, Y. J.; Ziller, J. W.; Yano, J.; Borovik, A. S. *J. Am. Chem. Soc.* **2012**, *134*, 17526−17535.

(13) Donoghue, P. J.; Tehranchi, J.; Cramer, C. J.; Sarangi, R.; Solomon, E. I.; Tolman, W. B. *J. Am. Chem. Soc.* **2011**, *133*, 17602−17605.

(14) Pfaff, F. F.; Heims, F.; Kundu, S.; Mebs, S.; Ray, K. *Chem. Commun.* **2012**, *48*, 3730−3732.

(15) Pirovano, P.; Farquhar, E. R.; Swart, M.; Fitzpatrick, A. J.; Morgan, G. G.; McDonald, A. R. *Chem. - Eur. J.* **2015**, *21*, 3785−3790.

(16) Corona, T.; Pfaff, F. F.; Acuña-Parés, F.; Draksharapu, A.; Whiteoak, C. J.; Martin-Diaconescu, V.; Lloret-Fillol, J.; Browne, W. R.; Ray, K.; Company, A. *Chem. - Eur. J.* **2015**, *21*, 15029−15038.

(17) Patra, A. K.; Mukherjee, R. *Inorg. Chem.* **1999**, *38*, 1388−1393.

(18) de Oliveira, F. T.; Chanda, A.; Banerjee, D.; Shan, X.; Mondal, S.; Que, L.; Bominaar, E. L.; Münck, E.; Collins, T. J. *Science* **2007**, *315*, 835−838.

(19) Ghosh, M.; Singh, K. K.; Panda, C.; Weitz, A.; Hendrich, M. P.; Collins, T. J.; Dhar, B. B.; Sen Gupta, S. *J. Am. Chem. Soc.* **2014**, *136*, 9524−9527.

(20) Taguchi, T.; Gupta, R.; Lassalle-Kaiser, B.; Boyce, D. W.; Yachandra, V. K.; Tolman, W. B.; Yano, J.; Hendrich, M. P.; Borovik, A. S. *J. Am. Chem. Soc.* **2012**, *134*, 1996−1999.

(21) Lacy, D. C.; Gupta, R.; Stone, K. L.; Greaves, J.; Ziller, J. W.; Hendrich, M. P.; Borovik, A. S. *J. Am. Chem. Soc.* **2010**, *132*, 12188−12190.

(22) Nagataki, T.; Ishii, K.; Tachi, Y.; Itoh, S. *Dalton Trans.* **2007**, 1120−1128.

(23) Nagataki, T.; Tachi, Y.; Itoh, S. *Chem. Commun.* **2006**, 4016−4018.

(24) Morimoto, Y.; Bunno, S.; Fujieda, N.; Sugimoto, H.; Itoh, S. *J. Am. Chem. Soc.* **2015**, *137*, 5867−5870.

(25) Yoon, H.; Wagler, T. R.; O'Connor, K. J.; Burrows, C. J. *J. Am. Chem. Soc.* **1990**, *112*, 4568−4570.

(26) Burrows, C. J.; Muller, J. G.; Poulter, G. T.; Rokita, S. E. *Acta Chem. Scand.* **1996**, *50*, 337−344.

(27) Grill, J. M.; Ogle, J. W.; Miller, S. A. *J. Org. Chem.* **2006**, *71*, 9291−9296.

(28) Draksharapu, A.; Codolà, Z.; Gómez, L.; Lloret-Fillol, J.; Browne, W. R.; Costas, M. *Inorg. Chem.* **2015**, *54*, 10656−10666.

(29) Liu, W.; Groves, J. T. *J. Am. Chem. Soc.* **2010**, *132*, 12847−12849.

(30) Yang, N.; Reiher, M.; Wang, M.; Harmer, J.; Duin, E. C. *J. Am. Chem. Soc.* **2007**, *129*, 11028−11029.

(31) Huang, Y. H.; Park, J. B.; Adams, M. W. W.; Johnson, M. K. *Inorg. Chem.* **1993**, *32*, 375−376.

(32) Sastri, C. V.; Seo, M. S.; Park, M. J.; Kim, K. M.; Nam, W. *Chem. Commun.* **2005**, 1405−1407.

(33) Nakazawa, J.; Terada, S.; Yamada, M.; Hikichi, S. *J. Am. Chem. Soc.* **2013**, *135*, 6010−6013.

(34) Cong, Z.; Yanagisawa, S.; Kurahashi, T.; Ogura, T.; Nakashima, S.; Fujii, H. *J. Am. Chem. Soc.* **2012**, *134*, 20617−20620.

(35) Sarangi, R. *Coord. Chem. Rev.* **2013**, *257*, 459−472.

(36) Penner-Hahn, J. E. *Coord. Chem. Rev.* **2005**, *249*, 161−177.

(37) Yano, J.; Yachandra, V. K. *Photosynth. Res.* **2009**, *102*, 241−254.

(38) Westre, T. E.; Kennepohl, P.; DeWitt, J. G.; Hedman, B.; Hodgson, K. O.; Solomon, E. I. *J. Am. Chem. Soc.* **1997**, *119*, 6297−6314.

(39) Colpas, G. J.; Maroney, M. J.; Bagyinka, C.; Kumar, M.; Willis, W. S.; Suib, S. L.; Baidya, N.; Mascharak, P. K. *Inorg. Chem.* **1991**, *30*, 920−928.

(40) Kau, L. S.; Spira-Solomon, D. J.; Penner-Hahn, J. E.; Hodgson, K. O.; Solomon, E. I. *J. Am. Chem. Soc.* **1987**, *109*, 6433−6442.

(41) Blusch, L. K.; Mitevski, O.; Martin-Diaconescu, V.; Pröpper, K.; DeBeer, S.; Dechert, S.; Meyer, F. *Inorg. Chem.* **2014**, *53*, 7876−7885.

(42) Scott, R. A.; Eidsness, M. K. *Comments Inorg. Chem.* **1988**, *7*, 235−267.

(43) Gu, W.; Wang, H.; Wang, K. *Dalton Trans.* **2014**, *43*, 6406−6413.
(44) Ray, K.; DeBeer George, S.; Solomon, E. I.; Wieghardt, K.; Neese, F. *Chem. - Eur. J.* **2007**, *13*, 2783−2797.
(45) In the presence of acetic acid, NaOCl becomes HOCl (the energy balance for NaOCl + AcOH → NaOAc + HOCl is −11 kcal·mol^{-1}), the latter being the oxidant used to calculate the thermodynamics.
(46) Martin-Diaconescu, V.; Gennari, M.; Gerey, B.; Tsui, E.; Kanady, J.; Tran, R.; Pécaut, J.; Maganas, D.; Krewald, V.; Gouré, E.; Duboc, C.; Yano, J.; Agapie, T.; Collomb, M.-N.; DeBeer, S. *Inorg. Chem.* **2015**, *54*, 1283−1292.
(47) Krewald, V.; Lassalle-Kaiser, B.; Boron, T. T.; Pollock, C. J.; Kern, J.; Beckwith, M. A.; Yachandra, V. K.; Pecoraro, V. L.; Yano, J.; Neese, F.; DeBeer, S. *Inorg. Chem.* **2013**, *52*, 12904−12914.
(48) Garribba, E.; Micera, G. *J. Chem. Educ.* **2006**, *83*, 1229.
(49) Hazra, S.; Naskar, S.; Mishra, D.; Gorelsky, S. I.; Figgie, H. M.; Sheldrick, W. S.; Chattopadhyay, S. K. *Dalton Trans.* **2007**, 4143−4148.
(50) Singh, A. K.; Balamurugan, V.; Mukherjee, R. *Inorg. Chem.* **2003**, *42*, 6497−6502.
(51) Rajput, A.; Mukherjee, R. *Coord. Chem. Rev.* **2013**, *257*, 350−368.
(52) Stoll, S.; Schweiger, A. *J. Magn. Reson.* **2006**, *178*, 42−55.
(53) Krejčik, M.; Daněk, M.; Hartl, F. *J. Electroanal. Chem. Interfacial Electrochem.* **1991**, *317*, 179−186.
(54) Newville, M. *J. Synchrotron Radiat.* **2001**, *8*, 96−100.
(55) Ravel, B.; Newville, M. *J. Synchrotron Radiat.* **2005**, *12*, 537−541.
(56) Rehr, J. J.; Albers, R. C. *Rev. Mod. Phys.* **2000**, *72*, 621−654.
(57) Banaszak, K.; Martin-Diaconescu, V.; Bellucci, M.; Zambelli, B.; Rypniewski, W.; Maroney, M. J.; Ciurli, S. *Biochem. J.* **2012**, *441*, 1017−1026.
(58) Martin-Diaconescu, V.; Bellucci, M.; Musiani, F.; Ciurli, S.; Maroney, M. J. *JBIC, J. Biol. Inorg. Chem.* **2012**, *17*, 353−361.
(59) Zambelli, B.; Berardi, A.; Martin-Diaconescu, V.; Mazzei, L.; Musiani, F.; Maroney, M. J.; Ciurli, S. *JBIC, J. Biol. Inorg. Chem.* **2014**, *19*, 319−334.
(60) Herbst, R. W.; Perovic, I.; Martin-Diaconescu, V.; O'Brien, K.; Chivers, P. T.; Pochapsky, S. S.; Pochapsky, T. C.; Maroney, M. J. *J. Am. Chem. Soc.* **2010**, *132*, 10338−10351.
(61) *Gaussian 09, Revision D.01*; Frisch, M. J.; Trucks, G. W.; Schlegel, H. B.; Scuseria, G. E.; Robb, M. A.; Cheeseman, J. R.; Scalmani, G.; Barone, V.; Mennucci, B.; Petersson, G. A.; Nakatsuji, H.; Caricato, M.; Li, X.; Hratchian, H. P.; Izmaylov, A. F.; Bloino, J.; Zheng, G.; Sonnenberg, J. L.; Hada, M.; Ehara, M.; Toyota, K.; Fukuda, R.; Hasegawa, J.; Ishida, M.; Nakajima, T.; Honda, Y.; Kitao, O.; Nakai, H.; Vreven, T.; Montgomery, J. A., Jr.; Peralta, J. E.; Ogliaro, F.; Bearpark, M.; Heyd, J. J.; Brothers, E.; Kudin, K. N.; Staroverov, V. N.; Kobayashi, R.; Normand, J.; Raghavachari, K.; Rendell, A.; Burant, J. C.; Iyengar, S. S.; Tomasi, J.; Cossi, M.; Rega, N.; Millam, M. J.; Klene, M.; Knox, J. E.; Cross, J. B.; Bakken, V.; Adamo, C.; Jaramillo, J.; Gomperts, R.; Stratmann, R. E.; Yazyev, O.; Austin, A. J.; Cammi, R.; Pomelli, C.; Ochterski, J. W.; Martin, R. L.; Morokuma, K.; Zakrzewski, V. G.; Voth, G. A.; Salvador, P.; Dannenberg, J. J.; Dapprich, S.; Daniels, A. D.; Farkas, Ö.; Foresman, J. B.; Ortiz, J. V.; Cioslowski, J.; Fox, D. J. Gaussian, Inc.: Wallingford, CT, 2009.
(62) Becke, A. D. *J. Chem. Phys.* **1993**, *98*, 1372−1377.
(63) Becke, A. D. *J. Chem. Phys.* **1993**, *98*, 5648−5652.
(64) Schaefer, A.; Huber, C.; Ahlrichs, R. *J. Chem. Phys.* **1994**, *100*, 5829−5835.
(65) Marenich, A. V.; Cramer, C. J.; Truhlar, D. G. *J. Phys. Chem. B* **2009**, *113*, 6378−6396.
(66) Grimme, S.; Ehrlich, S.; Goerigk, L. *J. Comput. Chem.* **2011**, *32*, 1456−1465.
(67) O'Boyle, N. M.; Tenderholt, A. L.; Langner, K. M. *J. Comput. Chem.* **2008**, *29*, 839−845.
(68) Lu, T.; Chen, F. *J. Comput. Chem.* **2012**, *33*, 580−592.
(69) Neese, F. *Wiley Interdisciplinary Reviews: Computational Molecular Science* **2012**, *2*, 73−78.
(70) DeBeer George, S.; Petrenko, T.; Neese, F. *Inorg. Chim. Acta* **2008**, *361*, 965−972.
(71) Roemelt, M.; Beckwith, M. A.; Duboc, C.; Collomb, M.-N.; Neese, F.; DeBeer, S. *Inorg. Chem.* **2012**, *51*, 680−687.
(72) Hirata, S.; Head-Gordon, M. *Chem. Phys. Lett.* **1999**, *314*, 291−299.
(73) Neese, F.; Olbrich, G. *Chem. Phys. Lett.* **2002**, *362*, 170−178.
(74) Schäfer, A.; Horn, H.; Ahlrichs, R. *J. Chem. Phys.* **1992**, *97*, 2571−2577.
(75) Klamt, A.; Schuurmann, G. *J. Chem. Soc., Perkin Trans. 2* **1993**, 799−805.

DOI: 10.1021/jacs.6b07544
J. Am. Chem. Soc. 2016, 138, 12987−12996